

Statistical comparison of substructures in pure aluminum before and after creep deformation, based on EBSD image data

Philipp Rieder^{a,*}, Lukas Petrich^a, Itziar Serrano-Munoz^b, Ricardo Fernández^c, Giovanni Bruno^b, Volker Schmidt^a

^a*Institute of Stochastics, Ulm University, Helmholtzstraße 18, Ulm, D-89069, Germany*

^b*Bundesanstalt für Materialforschung und -prüfung, Unter den Eichen 87, Berlin, D-12200, Germany*

^c*Centro Nacional de Investigaciones Metalúrgicas (CENIM), C.S.I.C., Av. de Gregorio del Amo 8, Madrid, E-28040, Spain*

Abstract

Electron backscatter diffraction (EBSD) images of extruded pure aluminum were statistically analyzed to investigate creep-induced subgrain structures after applying two different levels of creep stress, corresponding to the power law (PL) and power law breakdown (PLB) regimes. Kernel average misorientation analysis of EBSD measurements revealed 2D morphologies, which were subdivided by a multi-step segmentation procedure into subgranular arrangements. Various descriptors were employed to characterize the 'subgrains' quantitatively, including their size, shape, spatial arrangement and crystallographic orientation. In particular, the analysis of the orientations of subgrains was conducted by neglecting rotations around the loading axis. This approach facilitated the individual investigation of the {001} and {111} subgrain families with respect to the loading axis for the three investigated stress levels. For the PL regime, the statistical analysis of subgrain descriptors computed from segmented image data revealed a similar degree of strain accumulation for {111} and {001} subgrains. In contrast, for the PLB regime, the analyzed descriptors indicate that {111} subgrains tend to accumulate significantly more strain than {001} ones. These observations suggest that the mechanisms leading to PLB may be associated with strain localization dependent on intergranular stress, hindering the recovery process within {111} grains.

Keywords: Dislocation-climb-controlled creep, pure aluminum, electron backscatter diffraction (EBSD), kernel average misorientation (KAM), segmentation, subgrain, geometric descriptor, crystallographic descriptor, quantification, statistical image analysis

1. Introduction

For about a century, scientists have been investigating creep phenomena. Although countless articles with interesting insights to this topic have been published, see e.g. Andrade (1910); Garofalo (1965); Sherby and Burke (1968); Kassner (1984); Wilshire and Evans (1985); Ashby (1970); Arzt and Rösler (1988); Fernández et al. (2016, 2018); Prager (2000); Takeuchi et al.

*Corresponding author. E-mail address: philipp.rieder@uni-ulm.de

(1978); Kassner (2015); Evans and Harrison (1979), creep processes are to date not fully understood, in particular due to a lack of quantitative statistical analysis based on high-quality image data describing these processes. The aim of the present paper is to improve this unsatisfactory situation.

Over the years, several models describing the steady-state strain rate $d\varepsilon/dt$ in dependency of the applied stress σ were introduced. Among others, models described by a power-law dependence of the strain rate on applied stress are popular and widely accepted (Sherby and Burke, 1968). The power-law creep equation is supported by experimental data, but fails describing dislocation-climb-controlled creep occurring at high stress levels, known as the power law breakdown (PLB) regime (Kassner and Ermagan, 2019). At such stress levels the stress exponent is no longer constant, but increases with increasing stress. Despite the lack of a general consensus on the mechanism inducing the PLB, it is well accepted that the spatial distribution, size, and amount of stored dislocations are key parameters to the further elucidation of mechanisms governing creep resistance in metals.

The influence of intragranular stresses (type III) on the macroscopic creep response is extensively documented in the literature, see e.g. Caillard and Martin (1982); Hasegawa et al. (1972); Cadek (1987). Intragranular stresses result from the formation of different regions within a grain. Such regions contain different dislocation densities resulting from pile-ups at the subgrain walls, whereas the subgrain interior remains relatively free of dislocations. On the other hand, the influence of *intergranular* stress (type II) on creep resistance has just recently started to be addressed (see e.g., Chen et al. (2014); Mamun et al. (2021); Serrano-Munoz et al. (2022); Fernández et al. (2023)). The elastic and plastic deformation of a single grain is controlled by its crystallographic orientation, as well as by the orientation and deformation state of grains located in its vicinity, because of continuum compatibility. Intergranular interactions become even more significant when the material has been subjected to plastic pre-straining, as is the case of mechanical processing such as extrusion. Using different levels of pre-straining prior to creep tests has been reported to influence the rates of creep strain accumulation (Wilshire and Willis, 2004).

To analyze accumulated strain in materials, a suitable method is the so-called kernel average misorientation (KAM) applied on electron backscatter diffraction (EBSD) data, as outlined in several studies (Wright et al., 2011; Schwartz et al., 2009; Muránsky et al., 2019; Subedi et al., 2015; Wright et al., 2015). The segmentation of such KAM data is typically performed by experts, which is a time consuming and subjective task. On the other hand, there are segmentation approaches utilizing machine learning approaches to automatically segment specific structures in KAM data, yielding impressive results, see Martinez Ostormujof et al. (2022). However, such supervised segmentation methods require a manually labeled data set for training. An alternative approach is to utilize classical image processing techniques, such as a watershed algorithm, to segment granular structures from EBSD data (see e.g., McAuliffe et al. (2020); Jangid et al. (2022)). The present paper adapts such unsupervised methods into a multi-step image processing algorithm to effectively segment intragranular dislocation structures observed through EBSD and KAM computations.

Following the steps set forward in Serrano-Munoz et al. (2022), the resulting segmented structures, referred to as subgrains, are subjected to a comprehensive statistical analysis encompassing size, shape, spatial arrangement and crystal orientation descriptors of subgrains. Notably, an innovative methodology was developed to analyze crystallographic orientations by disregarding rotations around the loading axis of the creep experiment. This approach enables the representation of orientations in a manner consistent with their representation in an orientation mapping with respect to the loading axis. By employing this approach, subgrains closely

aligned with {001} and {111} orientations (with respect to the loading axis) were identified. Statistical data analysis was then conducted to assess their quantitative differences across the three investigated stress levels. The findings derived from this analysis provide further insights into the mechanisms behind the formation of creep-induced subgrain structures, contributing to a deeper understanding of these phenomena.

2. Materials, creep experiment and acquisition of image data

2.1. Materials

The specimens considered in the present work were produced out of a pure 99.8% aluminum bar with a diameter of 7 mm. They were manufactured at a pressure of 400 MPa and an extrusion temperature of 800 K. The yield stress corresponding to the material at room temperature is at 48 MPa.

2.2. Creep testing

The raw material was machined into cylindrical samples with a length of 10 mm, a diameter of 3 mm and were provided threaded heads, where the tensile axis was aligned parallel to the extrusion direction of the raw material. During the creep testing, we ensured a constant stress by using an Andrade cam, which compensates the decreasing sample section while the creep tensile deformation progresses. The elongation of the specimen during the creep experiment was reported as a function of time, by two digital strain gauges (SOLARTRON model DP/5/S) with a sensitivity of 0.2 μm . The sample clamping system, as well as the strain gauges suppressed the contribution of the machine and the grips from the sample creep strain. The creep experiments were conducted by applying stress levels of 21 MPa (corresponding to the region where dislocation-climb-controlled power-law creep is dominant) and 29 MPa (corresponding to the power-law breakdown regime) at a temperature of 573 K. The samples were heated at a constant heating rate of 100 K/h from room temperature to 573 K, soaked for 1 h and strained up to 0.025. To investigate the dislocation structures at each stress level, the specimens were cooled down rapidly by using an air jet. During the approximately 3 min of cooling, the samples were still exposed to the stress. The cooling corresponds to an effective cooling rate of around 6000 K/h. Even if diffusion still occurs during and after the cooling process, we assume dislocation structures, which are justifiable similar to the ones during creep deformation (Caillard and Martin, 1987; Yavari et al., 1981).

2.3. EBSD sample preparation and measurements

The samples were embedded in resin before being ground down to a diameter of approximately 1.5 mm. Afterwards, the surfaces were ground with SiC paper, polished with diamond slurries to 3 μm and polished finally with 0.02 μm colloidal silica suspension for 10 min, to remove possible residual deformations caused by the prior preparation steps.

The EBSD measurements were conducted with a field-emission gun scanning electron microscope (LEO 1530VP, Zeiss, Germany) running with an acceleration voltage of 20 kV and a probe current of 7 – 8 nA in high-pressure mode, at a working distance of 16 – 17 mm and using an objective aperture of 120 μm . Two conditions were established for the processing of the EBSD data: (i) the misorientation between neighbouring grains had to be greater than 5°, and (ii) each grain had to contain at least 2 data points. Note that the orientation raw data were denoised

using a total-variation-based filter implemented with image analysis routines. For further details on the EBSD pattern acquisition and evaluation, we refer to Serrano-Munoz et al. (2022).

To identify regions containing grains whose crystal orientation is in the vicinity of {001}, {011} and {111} directions relative to the loading direction (Y-axis), an EBSD map was first acquired at $\times 250$ magnification with a step size of $2.37 \mu\text{m}$. Regions containing at least one {001} grain neighbouring a {111} grain were then selected for further analysis. Such analysis was carried out at $\times 1000$ magnification with a step size of $0.29 \mu\text{m}$, resulting in a measured area of $152 \times 114 \mu\text{m}$. Besides the EBSD maps corresponding to the gauge region of the specimen, analyses were also conducted in its grip area. It is assumed that the grip did not undergo creep, but only the annealing heat treatment at 573 K. Therefore, the microstructural evolution at the grips should be the same for the samples crept at 21 MPa and 29 MPa. Hereafter, the results corresponding to the grip region of the sample crept at 21 MPa are referred to as the extruded+annealed condition (E+A).

For gauge regions of both, 21 MPa and 29 MPa, five cutouts were measured each, while six cutouts were considered for the grip. In the statistical analysis considered in Section 5, all cutouts corresponding to one stress condition were considered as one population.

2.4. Processing of image data

From image data¹, acquired by EBSD measurements we derived pixelwise information about the local crystallographic orientations of the samples considered (which possess a cubic crystal symmetry). In the following we represent an orientation $O \in \text{SO}_3$ as a pair of axis and angle, i.e.,

$$O = (\mathbf{r}, \omega), \quad (1)$$

where SO_3 denotes the group of all rotations in \mathbb{R}^3 , $\mathbf{r} \in \mathbb{R}^3$ is a unit vector of length 1, called the *axis of rotation* and $\omega \in [0, \pi)$, the *angle of rotation*. For the conversion of different representations of rotations into each other, we refer to Rowenhorst et al. (2015).

Without loss of generality, we assume that all orientations are transformed into a fundamental zone, i.e., all orientations that are equivalent under the crystal symmetry are identified with one unique orientation. Furthermore, in the present paper we assume that after applying an arbitrary operation the resulting orientation is still located in the fundamental zone.

To quantify the difference between two orientations $O_1, O_2 \in \text{SO}_3$ we define the so-called *misorientation* between O_1 and O_2 as the rotation $M(O_1, O_2) = O_2 \circ O_1^{-1} \in \text{SO}_3$, where \circ denotes the composition of rotations. Using the axis-angle representation of rotations given in Eq. (1), we obtain

$$M(O_1, O_2) = (\mathbf{r}_{1,2}, \omega_{1,2}) \quad (2)$$

for some unit vector $\mathbf{r}_{1,2} \in \mathbb{R}^3$ and some angle $\omega_{1,2} \in [0, \pi)$, where $\omega_{1,2}$ is called the *misorientation angle*. Thus, in order to investigate the discrepancy between two orientations $O_1, O_2 \in \text{SO}_3$, we consider in the following just their misorientation angle $\omega_{1,2}$.

For detailed information about deriving misorientations from EBSD orientation maps, the reader is referred to Randle and Engler (2000).

¹In this paper, EBSD orientation maps are referred to as image data. This wording is motivated by utilizing classical image processing methods, which can be applied to a wide range of similar problems, not just those based on EBSD measurements.

3. Segmentation of subgrains structures

The aim of this section is to describe the procedure we used to detect areas in the EBSD data that are homogeneous with respect to their crystallographic orientation. To achieve this goal, we first segmented the pixel grid $W = \{1, \dots, w\} \times \{1, \dots, h\}$ of the EBSD data with width w and height h into a certain number of *grains*. Such grains were computed with the software MTEX 5.8.0 (Bachmann et al., 2011) in MATLAB R2021a, i.e., we determined subsets $G_1, \dots, G_n \subset W$ of the pixel grid W such that $\bigcup_{i=1}^n G_i = W$, where $G_i \cap G_j = \emptyset$ for all $i, j \in \{1, \dots, n\}$ with $i \neq j$, and the misorientation angles between the crystallographic orientation of each pixel $\mathbf{x} \in G_i$ and those of its neighbors in G_i do not exceed 5° for all $i \in \{1, \dots, n\}$. Further we ensured that each grain G consists of at least 5 pixels and denoised the EBSD data after the segmentation by applying a so-called halfquadratic filter, which is based on total variation and is provided by MTEX.

3.1. Kernel average misorientation

In a second step we determined dislocation substructures within the grains. For this, we considered the kernel average misorientation (KAM) (Hielscher et al., 2019), i.e., using the MTEX software we computed the mean misorientation angle between the crystallographic orientation of each pixel $\mathbf{x} \in W$ and those of its neighbors in the set $N(\mathbf{x}) \subset W$, where $N(\mathbf{x})$ denotes the 4-neighborhood of \mathbf{x} within its grain. Thus, pixels that are not assigned to the same grain as \mathbf{x} are not considered in the computation of its KAM value $\kappa(\mathbf{x})$, formally defined by

$$\kappa(\mathbf{x}) = \frac{1}{|N(\mathbf{x})|} \sum_{\mathbf{y} \in N(\mathbf{x})} \omega_{\mathbf{x}, \mathbf{y}},$$

where $|\cdot|$ denotes the cardinality and $\omega_{\mathbf{x}, \mathbf{y}}$ is the misorientation angle between the crystallographic orientations of \mathbf{x} and \mathbf{y} .

The KAM values of an exemplary sample cutout are visualized in Fig. 1a as a grayscale image with values between 0 and 255. A visualization of rescaled KAM values of the same cutout, together with grain boundaries (red lines) directly deduced from EBSD data, is given in Fig. 1b, see Section 3.2 below for details. Intuitively, one can think of the image of KAM values as gradient image, where large values (bright lines) indicate an abrupt change in the crystallographic orientation. On the other hand, dark areas in Fig. 1b correspond to regions that are relatively homogeneous in their crystallographic orientation. These homogeneous areas will be called *subgrains* in the following.

3.2. Processing of KAM image data

To determine the subgrains with methods of image processing, we first enhanced the contrast of the KAM image by removing the outlier KAM values in the grayscale image. For this, we set KAM values smaller than the 5%-quantile to 0 and values greater than the 95%-quantile to 255. KAM values between the 5%– and 95%-quantile were then rescaled linearly to integers between 0 and 255, see Fig. 1b.

The remaining steps of image processing were conducted in python 3.7 and, if not stated otherwise, with scikit-image 0.18.3, see Van der Walt et al. (2014). First, to achieve a more homogeneous contrast between bright and dark pixels, from the rescaled KAM image a Gaussian blurred copy of it was subtracted, see Fig. 1c. For the Gaussian blurring a standard deviation $\sigma = 1.5$ turned out to be a reasonable choice. Finally, we binarized the grayscale image obtained

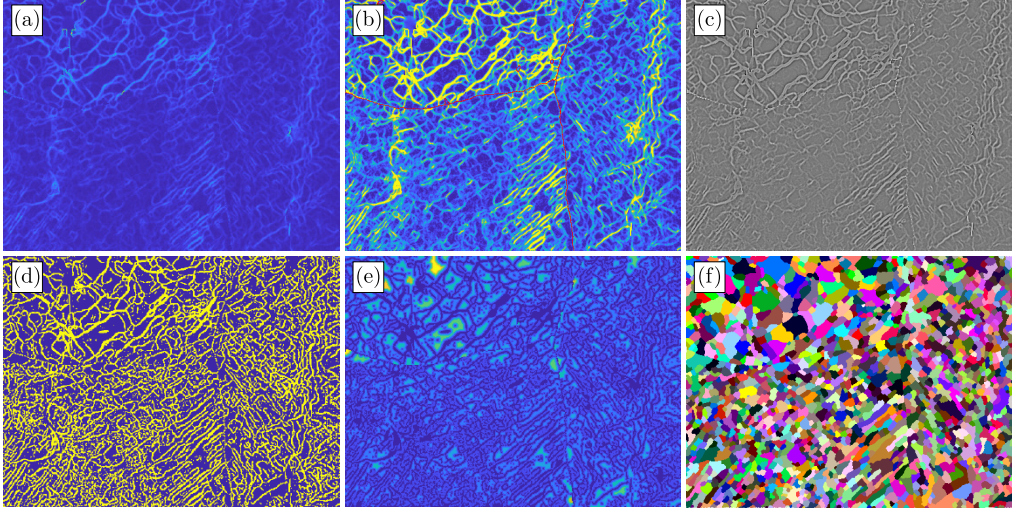


Figure 1: Workflow of image processing steps, visualized for an exemplary sample cutout which was exposed to a stress level of 21 MPa. Figs. 1a and b show the raw and rescaled KAM values. Note, that the red lines in Fig. 1b indicate the boundaries of the grains. Fig. 1c presents the KAM values subtracted by a blurred copy. The final segmentation (Fig. 1f) is obtained after binarization (Fig. 1d) and morphological reconstruction (Fig. 1e). For visualization purposes random colors are applied in Fig. 1f.

in this way using an Otsu rank filter, which is a local version of Otsu’s method (Otsu, 1979; Gonzalez and Woods, 2008) providing a local threshold for each pixel $\mathbf{x} \in W$. For this, we took a 25×25 neighborhood of \mathbf{x} within the sampling window W into account. The binarized KAM image $I = \{I(\mathbf{x}), \mathbf{x} \in W\}$ was obtained by setting the values of those pixels to 1, where the grayscale values (after subtracting the blurred copy) were at least equal to the local Otsu threshold. These pixels are referred to as foreground pixels, while the values of the remaining pixels were set to 0, representing the background pixels, see Fig. 1d.

3.3. Segmentation of grains into subgrains

Note that, by definition, the maximum of misorientation angles between the crystallographic orientation of a pixel belonging to a grain boundary and those of its neighbors on the pixel grid W is larger than 5° . This indicates a rapid change in the crystallographic orientation at grain boundaries. In the following we explain how a variant of the famous watershed algorithm (Beucher and Meyer, 1993) can be applied in order to further decompose each of the grains $G_1, \dots, G_n \subset W$ into subgrains, using the information about their inner grain structure provided by the binarized KAM image derived in Section 3.2.

First, for each grain $G \subset W$, we computed the Euclidean distance transformation $D_G = \{D(\mathbf{x}), \mathbf{x} \in G\}$ of the part $I_G = \{I(\mathbf{x}), \mathbf{x} \in G\}$ of the binarized KAM image I that corresponds to G (using SciPy 1.7.3. (Virtanen et al., 2020)). To each background pixel $\mathbf{x} \in G$ of the binary image I_G its distance to the closest foreground pixel in I_G was assigned. Then, the usual roadmap to segment a binary image would be to take the local maxima of its Euclidean distance transformation as markers for a marker-based watershed transformation (Gonzalez and Woods, 2008; Beucher and Meyer, 1993). However, in the present application this would have led to an oversegmentation, i.e., too many and too small subgrains would have been obtained. There-

fore, we considered a so-called morphological reconstruction (Vincent, 1993; Zheng and Hryciw, 2016), which is a method to reduce the set of local maxima used for the marker-based watershed transformation. Roughly speaking, the morphological reconstruction “merges” the locations of two neighboring local maxima $d_1 \geq d_2 > 0$ of D_G if $\frac{w}{d_2} \geq 1 - c$ for some $c \in (0, 1)$, where w denotes the value of D_G at the watershed ridge between d_1 and d_2 . In our application, it turned out that $c = 0.3$ led to suitable results, see Fig. 1e. For further details regarding this kind of morphological reconstruction, we refer to Zheng and Hryciw (2016).

The decomposition of grains into subgrains described above, needed some post-processing. Namely, for some threshold $a_{min} > 0$, regions consisting of less than a_{min} pixels were removed and their pixels were assigned to neighboring regions. For this, we considered a second watershed transformation with the remaining regions as markers and the minimum distances from deleted pixels to a remaining one. Putting $a_{min} = 10$, we obtained the final segmentation of grains into subgrains, see Fig. 1f. In the following, this final segmentation will be considered as a mapping $S : W \rightarrow \{1, \dots, N\}$, where $N \geq 1$ denotes the total number of subgrains. Here, each pixel $\mathbf{x} \in W$ is mapped to an integer $S(\mathbf{x})$ with $1 \leq S(\mathbf{x}) \leq N$, which indicates the label of the subgrain, \mathbf{x} is assigned to. Furthermore, by $S_n = \{\mathbf{x} \in W : S(\mathbf{x}) = n\}$ we denote the subgrain with label n for all $n = 1, \dots, N$.

4. Statistical analysis of segmented data

We now recall the definition of several geometric and crystallographic descriptors, which will be used in order to analyze the (irregularly shaped) subgrains derived in Section 3. The obtained results will be discussed in Section 5 with regard to the different stress conditions the specimen was exposed to. Because of the two-dimensional nature of the EBSD data, only cross-sections of the 3D (sub-)grains can be considered. This has to be taken into account when interpreting the results presented in Section 5.

4.1. Geometric descriptors of subgrains

A fundamental descriptor of a subgrain $S \subset W$ is its area $a(S)$, which is given by the number of pixels assigned to S , i.e., $a(S) = |S|$.

The elongation $e(S)$ of a subgrain $S = \{\mathbf{x}_1, \dots, \mathbf{x}_m\} \subset W$ is given by the ratio of the (major and minor) axes lengths of the best fitting ellipse, which is determined by means of principle component analysis (PCA), see e.g. Hastie et al. (2009). For this, we consider the pixels $\mathbf{x}_1, \dots, \mathbf{x}_m$ belonging to S as a point cloud $\mathbf{x}_1 = (x_1, y_1), \dots, \mathbf{x}_m = (x_m, y_m)$ in \mathbb{R}^2 . In order to perform the PCA we compute the centroid $(\bar{x}, \bar{y}) \in \mathbb{R}^2$ of this point cloud, and the covariance matrix

$$K(S) = \begin{pmatrix} \frac{1}{m} \sum_{i=1}^m (x_i - \bar{x})^2 & \frac{1}{m} \sum_{i=1}^m (x_i - \bar{x})(y_i - \bar{y}) \\ \frac{1}{m} \sum_{i=1}^m (x_i - \bar{x})(y_i - \bar{y}) & \frac{1}{m} \sum_{i=1}^m (y_i - \bar{y})^2 \end{pmatrix},$$

together with its eigenvalues $\lambda_1, \lambda_2 > 0$, where $\lambda_1 \geq \lambda_2$, and the corresponding eigenvectors $\mathbf{a}_1 = (a_{11}, a_{12}), \mathbf{a}_2 = (a_{21}, a_{22}) \in \mathbb{R}^2$. Note that the vectors \mathbf{a}_1 and \mathbf{a}_2 point in the direction of the major and minor axes of the fitted ellipse, respectively, where the lengths $\ell_1(S)$ and $\ell_2(S)$ of these axes are given by $\ell_i(S) = 4\sqrt{\lambda_i}$ for $i = 1, 2$. Thus, the elongation $e(S) \in [0, 1]$ of a subgrain S , also called the aspect ratio of S , is given by

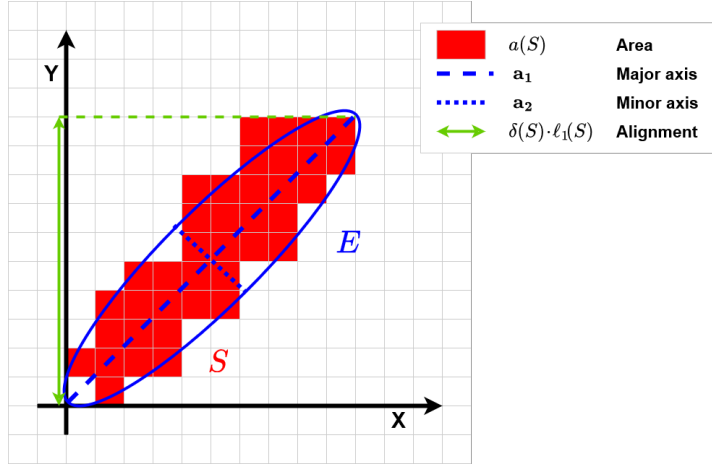


Figure 2: Schematic visualization of the geometric descriptors of a subgrain S with fitted ellipse E .

$$e(S) = \frac{\ell_2(S)}{\ell_1(S)} = \sqrt{\frac{\lambda_2}{\lambda_1}},$$

where $e(S) \approx 1$ indicates that the shape of S is not elongated and decreasing values of $e(S)$ correspond to more and more elongated subgrains.

Finally, we analyze the (spatial) orientation of subgrains, investigating the alignment $\delta(S) \in [0, 1]$ of a subgrain S with respect to the Y-axis of the coordinate system. More precisely, we consider the alignment of the eigenvector $\mathbf{a}_1 = (a_{11}, a_{12})$ with respect to the Y-axis, which is given by

$$\delta(S) = |\langle \mathbf{a}_1, \mathbf{e}_2 \rangle| = |a_{12}|,$$

where $\mathbf{e}_2 = (0, 1)^\top$ and $\langle \cdot, \cdot \rangle$ denotes the scalar product in \mathbb{R}^2 . Note that the Y-axis is the loading axis of the creep experiment described in Section 2.2. Thus, for a (non-circular) subgrain S an alignment of $\delta(S) = 1$ corresponds to an elongation of S parallel to the loading axis, whereas $\delta(S) = 0$ means that S is oriented along the X-axis. The geometric descriptors considered above are visualized in Fig. 2.

To further analyze the shapes of subgrains we considered two additional descriptors. First, the circularity factor $s(S) \in [0, 1]$ of a subgrain S is considered, which is given by

$$s(S) = \frac{2\sqrt{\pi a(S)}}{p(S)}.$$

Here $p(S)$ denotes the perimeter of S , which we determined by means of Croftons formula, implemented in scikit-image 0.18.3 (Van der Walt et al., 2014). Note that $2\sqrt{\pi a(S)}$ indicates the perimeter of a area-equivalent circle of S . A circularity factor $s(S) = 1$ indicates a perfect circle, where decreasing values of $s(S)$ stand for less spherical shapes. Due to discretization effects it can happen that $s(S) > 1$ for some S , which we set equal to 1.

Furthermore, we consider is the so-called convexity $c(S) \in [0, 1]$, which is given by

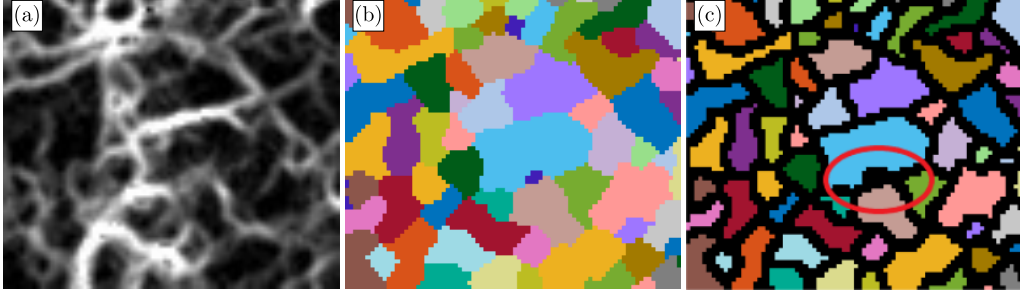


Figure 3: Cutout of a scaled KAM image (Fig. 3a) and its segmentation, before (Fig. 3b) and after erosion (Fig. 3c) with a 3×3 box. Note that small subgrains may vanish (red mark).

$$c(S) = \frac{a(S)}{a(q(S))},$$

where $q(S)$ denotes the discrete convex hull of S on the pixel grid W . Here, the value of $c(S) = 1$ corresponds to convex subgrains. For visualizations of circularity factor $s(S)$ and convexity $c(S)$ we refer to Fig. 6 of Furat et al. (2021).

4.2. Crystallographic descriptors of subgrains

We recall the segmentation procedure of scaled KAM images described in Section 3, see also Fig. 1. Subgrains are defined as homogeneous dark regions, surrounded by bright lines which indicate larger changes in the crystallographic orientation. These lines, having a width of at least one pixel, are used to determine the boundaries of subgrains. However, each pixel in the final segmentation (see Fig. 1f) is assigned to a subgrain and, consequently, the boundary has zero width. Determining descriptors of subgrains depending on their crystallographic orientation leads to the problem that the orientations of some boundary pixels can differ drastically from the ones of interior pixels. To exclude such effects we eroded each subgrain S by a 3×3 pixel box, see Fig. 3c. The eroded subgrain corresponding to S is denoted by S' in the following. For more details regarding the erosion of regions in digital images, we refer e.g. to Gonzalez and Woods (2008). Note that through the erosion approximately 1% of small subgrains vanished.

We also consider the so-called maximum intragranular misorientation angle $\omega_{\max}(S)$ for each subgrain $S \subset W$, as well as its counterpart $\omega'_{\max}(S)$ of the eroded subgrain $S' \subset S$. Formally, they are defined as

$$\omega_{\max}(S) = \max_{\mathbf{x} \in S} \omega_{\mathbf{x}} \quad \text{and} \quad \omega'_{\max}(S) = \max_{\mathbf{x} \in S'} \omega'_{\mathbf{x}}, \quad (3)$$

where $\omega_{\mathbf{x}}$ and $\omega'_{\mathbf{x}}$ denote the misorientation angles between the crystallographic orientation of \mathbf{x} and the mean crystallographic orientations of S and S' , respectively. Fig. 4 shows kernel density estimates of the probability distribution of the maximum intragranular misorientation angles $\omega_{\max}(S)$, $\omega'_{\max}(S)$, based on data computed for all (eroded and non-eroded) subgrains of the three samples (E+A, 21 MPa, 29 MPa) considered in the present paper.

By intuition it is clear that the maximum intragranular misorientation angle decreases by considering the eroded subgrain S' instead of the non-eroded one S . In fact, the inequality

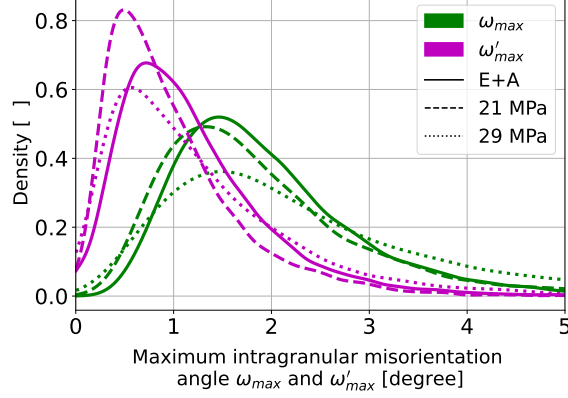


Figure 4: Probability densities of maximum intragranular misorientation angles for the three conditions (extruded+annealed, 21 MPa, 29 MPa). Green lines show the distribution of $\omega_{\max}(S)$ for non-eroded subgrains, whereas purple lines visualize the distribution of $\omega'_{\max}(S)$ for eroded subgrains.

$\omega'_{\max}(S) \leq \omega_{\max}(S)$ holds, because $S' \subset S$. In Fig. 4, one can observe a drastic decrease of the maximum intragranular misorientation angle within the subgrains by considering S' instead of S . This indicates a rapid change in the crystallographic orientation between the outer and the second outer layer of pixels of subgrains. Considering the corresponding mean values of the three stress conditions they nearly half when passing from non-eroded to eroded subgrains. Namely, the mean values decrease from from 2.00° to 1.19° for extruded+annealed, from 1.95° to 0.99° for 21 MPa, and from 2.49° to 1.28° for 29 MPa. Consequently we consider in the following the eroded subgrains S' for determining the crystallographic descriptors.

Besides investigating the influence of creep on the maximum intragranular misorientation angle $\omega'_{\max}(S)$ introduced in Eq. (3), we also consider the intragranular mean μ and variance σ^2 of misorientation angles of eroded subgrain S' . These characteristics are given by

$$\mu(S) = \frac{1}{|S'|} \sum_{x \in S'} \omega'_x \quad \text{and} \quad \sigma^2(S) = \frac{1}{|S'| - 1} \sum_{x \in S'} (\omega'_x - \mu(S))^2, \quad (4)$$

where ω'_x denotes the pixelwise misorientation angle introduced in Eq. (3). The two descriptors $\mu(S)$ and $\sigma^2(S)$ can be interpreted as the mean strain-accumulation and the strain-accumulation variance in the subgrain ensemble, respectively. Moreover, it is noteworthy that the crystallographic descriptors $\mu(S)$ and $\sigma^2(S)$ of eroded subgrains given in Eq. (4) play a similar role as the texture descriptors of segmented grayscale images considered in Furat et al. (2023).

In a previous paper, see Serrano-Munoz et al. (2022), the influence of creep on $\{111\}$ and $\{001\}$ families of grains was investigated. The difference between these two types of grains is their degree of alignment relative to the Y-axis and is motivated by EBSD orientation mapping with respect to the Y-axis (OM-Y). In Serrano-Munoz et al. (2022), as well as in the present paper, the Y-axis has been chosen because it coincides with the loading axis of the creep experiment described in Section 2.2. Mathematically speaking, an OM-Y is a mapping of a crystallographic orientation onto a certain spatial direction. More precisely, an orientation $O \in \text{SO}_3$ is mapped to the direction in the correspondingly rotated coordinate system (in other words, the direction in the crystal), which corresponds to the Y-axis in the (global) reference system. Thus, rotations

of O around the global Y-axis have no influence on its representation in the OM-Y. Note that the definition of $\{111\}$ and $\{001\}$ grains via the EBSD orientation coloring is a natural choice, because rotating the specimen around the loading axis in the experimental setup, changes the orientations with respect to the reference system, but has no influence on the results of the experiment. For the upcoming sections, let O_{111} and O_{001} denote the crystallographic orientation of elastically stiffer $\{111\}$ and softer $\{001\}$ grains, respectively.

A quantity describing the difference between the mean crystallographic orientation O' of an eroded subgrain S' and the reference orientations O_{111} or O_{001} is needed. Such a quantity should not depend on rotations around the loading axis. For this, we define $[O] = \{\tilde{O} \in \text{SO}_3 : \tilde{O}$ has the same OM-Y representation as $O\}$, the equivalence class of the rotation O with respect to an OM-Y. Since rotations around the Y-axis do not affect the OM-Y of a rotation, $[O]$ can be expressed as the set of rotations obtained by rotating O by any arbitrary angle around the Y-axis. More formally, this means that

$$[O] = \{\tilde{O} \in \text{SO}_3 : \tilde{O} = O \circ O_y, O_y \in \text{SO}_{3,y}\}, \quad (5)$$

where $\text{SO}_{3,y} \subset \text{SO}_3$ denotes the family of rotations around the Y-axis.

A suitable quantity to describe the difference between O' and O_{ref} , which is either O_{111} or O_{001} , is the minimum misorientation angle between O_{ref} and the equivalence class of O' , defined by

$$\omega_{\text{ref}}^*(S) = \min_{O \in [O']} f_\omega(M(O, O_{\text{ref}})) = \min_{O \in [O']} \omega, \quad (6)$$

where $f_\omega : \text{SO}_3 \rightarrow [0, \pi)$ maps an crystallographic orientation $O = (\mathbf{r}, \omega)$ onto the angle ω of its axis-angle representation. For sake of simplification, the descriptor $\omega_{\text{ref}}^*(S)$ will be called the misorientation angle with respect to O_{ref} . By plugging Equation (5) into Equation (6), we get the minimization problem

$$\omega_{\text{ref}}^*(S) = \min_{O' \in \text{SO}_{3,y}} f_\omega(M(O \circ O', O_{\text{ref}})) = \min_{O' \in \text{SO}_{3,y}} \omega,$$

which we solved with an interior point method (Byrd et al., 2000) implemented in MATLAB.

5. Results and discussion

Fig. 5 shows representative results of the EBSD orientation maps, KAM computation, and the segmentation of subgrains for each of the considered conditions. As reported in Serrano-Munoz et al. (2022), the qualitative evaluation of the KAM and segmentation maps allows us to state that the extrusion and annealing process induces the smallest subgrains. For the two creep conditions (21 MPa and 29 MPa), the $\{001\}$ grains appear contain larger subgrain structures, whereas the $\{111\}$ grains tend to accumulate larger amounts of strain. Furthermore, it turned out that the 29 MPa stress level induces higher spatial in-homogeneity of strain accumulation.

To bring further insight into how creep mechanisms are influencing the formation of subgrains, the geometric and crystallographic descriptors outlined in Section 4 were computed. It is noteworthy that all cutouts corresponding to a single stress condition were considered as one population.

To compare the effects of creep on $\{111\}$ and $\{001\}$ subgrains, we define the set S_{ref} , which contains all subgrains where the misorientation angle ω_{ref}^* with respect to O_{ref} is less than or equal to $\pi/9$ ($= 20^\circ$). Furthermore, for ease of understanding, we refer to

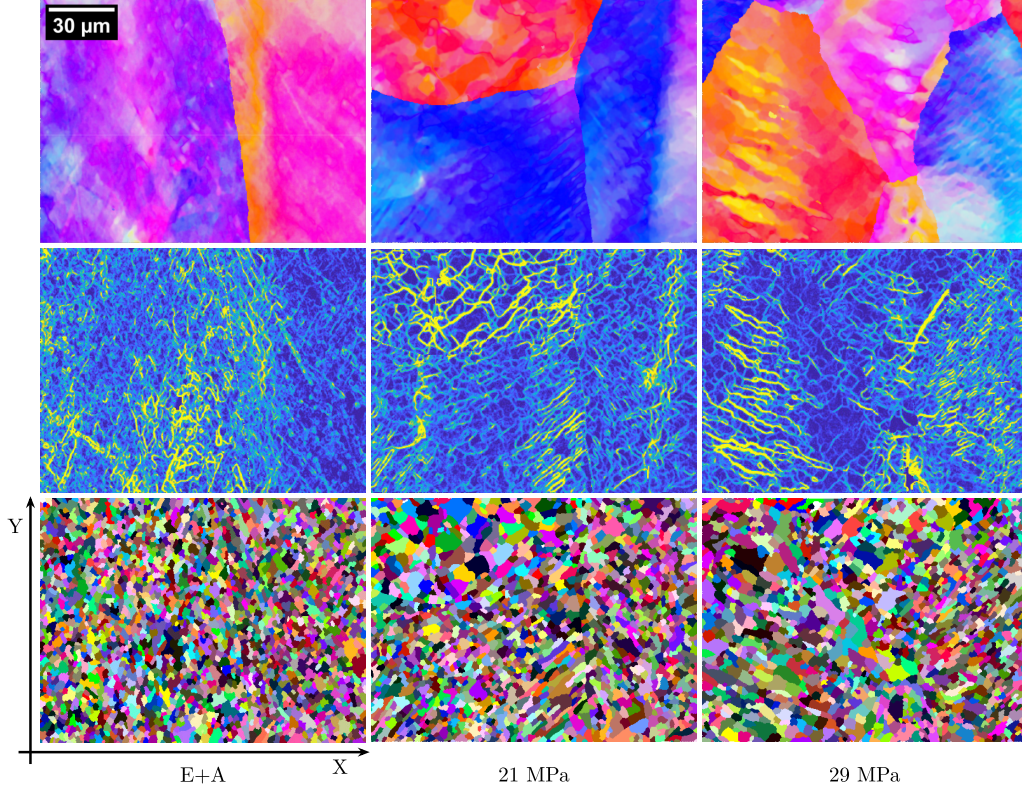


Figure 5: Comparison of representative EBSD grain orientation maps (top), the rescaled KAM values (middle), and the results of subgrain segmentation (bottom). To achieve optimal contrast between the segmented subgrains, they are mapped with false colors.

$$S_{111} = \{S : \omega_{111}^*(S) \leq \pi/9\} \quad \text{and} \quad S_{001} = \{S : \omega_{001}^*(S) \leq \pi/9\}$$

as $\{111\}$ and $\{001\}$ subgrains, respectively. Fig. 6 provides a visualization of the definition of S_{001} and S_{111} . For a qualitative comparison of S_{001} and S_{111} with respect to the different stress conditions, probability densities were determined for each descriptor, using (truncated) kernel density estimation².

Fig. 7 shows the probability densities corresponding to the size descriptors, namely the area $a(S)$ as well as the lengths of the major and minor axes $\ell_1(S)$ and $\ell_2(S)$. All three plots indicate that differences in size depending on the stress condition, as well as the crystal orientation. The visual impression is confirmed by the mean values of descriptors, shown in Table 1. Extrusion+annealing does not yield any significant differences in size between $\{111\}$ and $\{001\}$ grains. Given that the extrusion process causes the development of a $\{001\}+\{111\}$ fiber texture, and that $\{111\}$ grains are elastically stiffer than $\{001\}$ ones, one could expect the extrusion process to bring

²To set the bandwidth of the kernel density estimators, we used Silverman's rule of thumb (Silverman, 1986).

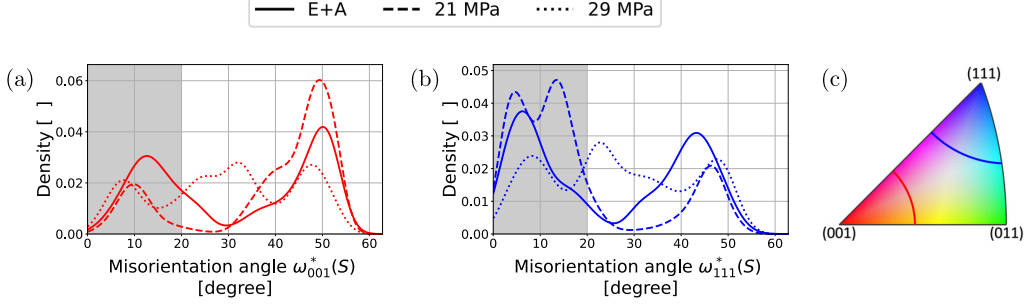


Figure 6: Figs. 6a and 6b show kernel density estimations of the misorientation angle with respect to $\omega_{001}^*(S)$ and $\omega_{111}^*(S)$, respectively. The shaded grey regions show the misorientation angles which are smaller than or equal to 20° and indicates S_{001} and S_{111} , respectively. Fig. 6c shows the orientations, which are considered as {001} (red) and {111} (blue) grains, visualized using an inverse pole figure color key.

	E+A		21 MPa		29 MPa	
	{001}	{111}	{001}	{111}	{001}	{111}
Area $a(s)$	7.637	7.19	12.101	9.825	11.536	8.896
Length of major axis $\ell_1(S)$	4.032	4.006	4.914	4.586	4.831	4.444
Length of minor axis $\ell_2(S)$	2.443	2.365	2.926	2.692	2.86	2.545
Elongation $e(S)$	0.430	0.417	0.418	0.420	0.421	0.407
Circularity factor $s(S)$	0.846	0.849	0.857	0.854	0.851	0.847
Convexity $c(S)$	0.862	0.865	0.880	0.874	0.873	0.87
Alignment with Y-axis $\delta(S)$	0.715	0.724	0.697	0.671	0.704	0.701
Mean misorientation angle $\mu(S)$	0.484	0.552	0.371	0.361	0.439	0.539
Intragranular variance $\sigma^2(S)$	0.082	0.103	0.067	0.056	0.102	0.121

Table 1: Mean values of geometric and crystallographic descriptors.

some size difference as a function of crystal orientation. It could be that the annealing during the creep testing has a homogenizing effect, bringing the size of the subgrain structures in these two types of grains to similar values. However, a detailed investigation of subgrain formation as induced by the extrusion process is beyond the scope of this work.

It is important to emphasize that different pre-strain levels in these two grain families induced by the extrusion process influence the strain accumulation during creep. Moreover, it is well known that the size of the creep-induced subgrain structures is strongly correlated with the creep stress level: the higher the creep stress, the finer the subgrain size (Sherby and Burke, 1968). Thus, the larger subgrain structures identified in {001} grains for both creep conditions are related to a higher stress associated with a load transference effect, due to the intergranular stress state. Such stress is of lower magnitudes in {001} grains than in {111} grains. This corroborates our interpretation made in Serrano-Munoz et al. (2022).

Figs. 8a-c show the probability densities corresponding to the shape descriptors (elongation $e(s)$, circularity factor $s(S)$ and convexity $c(S)$). No significant differences are observed between the three conditions or the two grain families. Also the mean values, standard deviations and skewnesses of these three descriptors are similar, see Table 1 as well as Tables A10 and A11 of

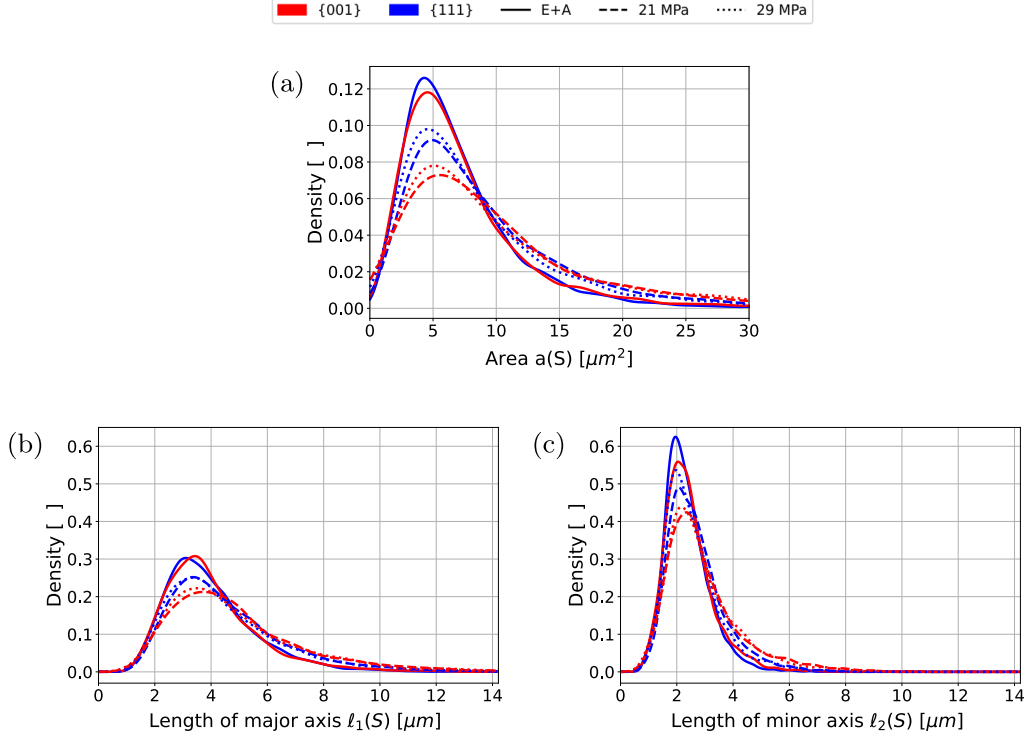


Figure 7: Probability densities of area $a(S)$ and the lengths of the major and minor axes $l_1(S)$, $l_2(S)$ of an ellipse fitted to {001} and {111} subgrains for the three conditions (extruded+annealed, 21 MPa, 29 MPa).

the Appendix. It has been proposed in Cadek (1987) that the intragranular stress measured in steady state creep of pure metals represents a level of internal backward stress acting in the soft regions (subgrain interior), whereas in the hard regions (subgrain walls) large, forward internal stresses act. These internal stresses would, therefore, lead to the same roundish morphology (the circularity mean is about 0.9). The only difference is induced by the stress magnitude on the spacing between the subgrain walls (i.e. the subgrain size).

Interestingly, the alignment of the subgrains major axis with the Y-axis $\delta(S)$, see Fig. 7c, indicates differences between the extruded+annealed condition and the two creep conditions, but not between the grain families. It is important to recall that the Y-axis is both the extrusion and the creep-loading direction. In fact, the alignment to the Y-axis is reduced after creep, most likely due to the recovery occurring during creep, which would tend to attenuate the directionality of the creep hardening process (i.e., the development of the subgrain structures). This concept has already been introduced in Serrano-Munoz et al. (2022), but at a speculative level. In the present paper it is better circumstantiated.

Fig. 9a shows the probability densities corresponding to the intragranular mean misorientation $\mu(S)$, i.e. the descriptor of strain-accumulation. In this case, there are differences between the three conditions, as well as between the {111} and {001} grains. {111} grains exhibit a slightly higher accumulation of strain in the extruded+annealed condition when compared to the {001}.

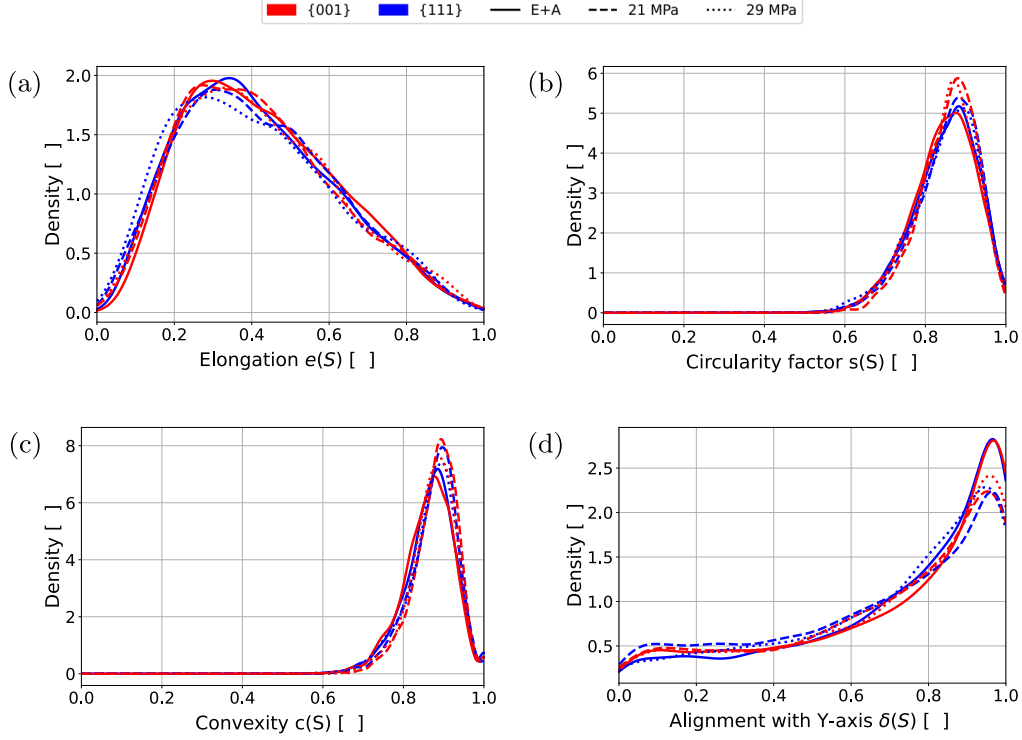


Figure 8: Probability densities of elongation $e(S)$, circularity factor $s(S)$, convexity $c(S)$ and alignment with Y-axis $\delta(S)$ of {001} and {111} subgrains for the three conditions (extruded+annealed, 21 MPa, 29 MPa).

As mentioned above, it is uncertain whether the recovery induced by the annealing process reduces the differences in strain accumulation between these two families. In any case, it is important to notice that the extruded+annealed condition exhibits the highest levels of strain accumulation. This is due to the fact that, during creep, the steady-state flow is a balance between the hardening process and dynamic recovery inducing annihilation of dislocations.

For the 21 MPa condition, the intragranular strain accumulation is similar for {111} and {001} grains. As expected, the strain accumulation is higher at 29 MPa compared to 21 MPa. Notably, {111} grains exhibited a considerably higher strain accumulation than {001} grains at 29 MPa. This strain accumulation dependence on crystal orientations as a function of stress is considered to correlate with the power law breakdown. In other words, at high stress creep range (29 MPa), as opposed to intermediate creep stress range (21 MPa), there is a localization of strain accumulation as a function of crystal orientation. Note that, as aforementioned, this crystal-orientation-based localization is originally driven by the extrusion-inherited intergranular stress state.

The evaluation of the intragranular variance $\sigma^2(S)$ (strain accumulation variance), shown in Fig. 9b, leads to a similar conclusion: the inhomogeneity of strain accumulation is greater at 29 MPa than at 21 MPa, especially within {111} grains. This could be indicative that the annihilation rate of climbing dislocations is lower in the power law breakdown regime.

By visual inspection, it is evident that the probability densities shown in Fig. 6 to 9 exhibit

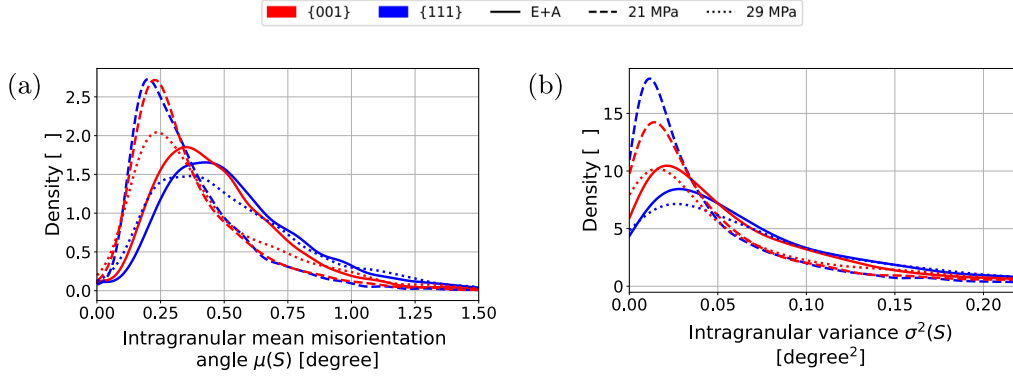


Figure 9: Probability densities of crystallographic descriptors of eroded {001} and {111} subgrains for the three conditions (extruded+annealed, 21 MPa, 29 MPa).

in the most cases clearly visible differences. To confirm this impression the reader is referred to Tables A1 to A9 of the Appendix. These tables present the p -values resulting from statistical tests, examining whether the descriptors follow different distributions for various stress levels and subgrain types.

6. Conclusions

In the present work, creep-induced subgrain structures formed in pure aluminum were quantitatively investigated by a statistical analysis based on segmented EBSD-KAM images. The segmentation procedure was designed to subdivide the granular structure of the crept material into subgrains by using various methods of image processing. To perform a comprehensive evaluation of the influence of thermo-mechanical history (e.g., extrusion+annealing and creep at 21 MPa, power law regime, and at 29 MPa, power law breakdown regime), several geometric and crystallographic descriptors, which characterize size, shape and strain accumulation, were determined for each subgrain.

Regarding creep mechanisms, it is observed that the intergranular stress state inherited from the extrusion process leads to larger subgrain sizes in {001} grains upon exposure to creep. Also, the alignment of the major axis of subgrains is slightly reduced after creep, most likely due to a relaxing effect induced by the creep recovery process. More importantly, it is observed that {111} grains tend to accumulate more strain than {001} grains at high stress creep (29 MPa), when compared to the intermediate creep stress range (21 MPa). Such variations in subgrain sizes are considered as indicators of increased strain inhomogeneity, occurring within the power law breakdown regime. This inference is drawn from the correlation between subgrain size and applied creep stress, a relationship supported by the research conducted by Sherby and Burke (1968). It is postulated that this inhomogeneity may be attributed to a hampered recovery process occurring within {111} grains.

Acknowledgements

This work was partially funded by the German Research Foundation (DFG) under project numbers BR 5199/5-1 and SCHM 997/37-1, as well as by the Bundesministerium für Bildung und Forschung (BMBF) under the grant number 01IS2109. The authors would like to thank Benedikt Prifling for his helpful comments regarding processing and analysis of image data. Gratitude is expressed to Romeo Saliwan-Neumann and Mareike Kirstein for their assistance during the EBSD measurements and sample preparation, respectively.

Data availability

The raw/processed data required to reproduce these findings cannot be shared at this time as the data also forms part of an ongoing study.

Conflict of interests

The author(s) declare no conflict of interests.

References

- E. N. D. C. Andrade. On the viscous flow in metals, and allied phenomena. *Proceedings of the Royal Society of London*, 84(567):1–12, 1910.
- E. Arzt and J. Rösler. The kinetics of dislocation climb over hard particles-II. Effects of an attractive particle-dislocation interaction. *Acta Metallurgica*, 36:1053–1060, 1988.
- M. Ashby. The deformation of plastically non-homogeneous materials. *The Philosophical Magazine*, 21:399–424, 1970.
- F. Bachmann, R. Hielscher, and H. Schaeben. Grain detection from 2d and 3d EBSD data - specification of the MTEX algorithm. *Ultramicroscopy*, 111:1720–1733, 2011.
- S. Beucher and F. Meyer. The morphological approach to segmentation: The watershed transformation. In E. R. Dougherty, editor, *Mathematical Morphology in Image Processing*, page 433–481. Marcel Dekker Inc, 1993.
- R. H. Byrd, J. C. Gilbert, and J. Nocedal. A trust region method based on interior point techniques for nonlinear programming. *Mathematical Programming*, pages 149–185, 2000.
- J. Cadek. The back stress concept in power law creep of metals: A review. *Materials Science and Engineering*, 94: 79–92, 1987.
- D. Caillard and J. Martin. Microstructure of aluminium during creep at intermediate temperature-II. In situ study of subboundary properties. *Acta Metallurgica*, 30:791–798, 1982.
- D. Caillard and J. Martin. New trends in creep microstructural models for pure metals. *Revue de Physique Appliquée*, 22:169–183, 1987.
- B. Chen, J. Hu, P. Flewitt, D. Smith, A. Cocks, and S. Zhang. Quantifying internal stress and internal resistance associated with thermal ageing and creep in a polycrystalline material. *Acta Materialia*, 67:207–219, 2014.
- W. Evans and G. Harrison. Validity of friction stress σ_0 measurements for high-temperature creep. *Metal Science*, 13: 346–350, 1979.
- R. Fernández, G. Bruno, and G. González-Doncel. Primary and secondary creep in aluminum alloys as a solid state transformation. *Journal of Applied Physics*, 120:085101, 2016.
- R. Fernández, G. Bruno, and G. González-Doncel. Fractal nature of aluminum alloys substructures under creep and its implications. *Journal of Applied Physics*, 123:145108, 2018.
- R. Fernández, G. Bokuchava, G. Bruno, I. Serrano-Munoz, and G. González-Doncel. On the dependence of creep-induced dislocation configurations on crystallographic orientation in pure Al and Al-Mg. *Journal of Applied Crystallography*, 2023. Under revision.
- O. Furat, D. P. Finegan, D. Diercks, F. Usseglio-Viretta, K. Smith, and V. Schmidt. Mapping the architecture of single lithium ion electrode particles in 3D, using electron backscatter diffraction and machine learning segmentation. *Journal of Power Sources*, 483:229148, 2021.
- O. Furat, T. Kirstein, T. Leißner, K. Bachmann, J. Gutzmer, U. A. Peuker, and V. Schmidt. Multidimensional characterization of particle morphology and mineralogical composition using CT data and R-vine copulas. *arXiv: 2301.07587*, 2023.

- F. Garofalo. *Fundamentals of Creep and Creep-Rupture in Metals*. MacMillan and Co., 1965.
- R. C. Gonzalez and R. E. Woods. *Digital Image Processing*. Prentice Hall, 2008.
- T. Hasegawa, Y. Ikeuchi, and S. Karashima. Internal stress and dislocation structure during sigmoidal transient creep of a copper–16 at.-% aluminium alloy. *Metal Science Journal*, 6:78–82, 1972.
- T. Hastie, R. Tibshirani, and J. Friedman. *The Elements of Statistical Learning: Data Mining, Inference, and Prediction*. Springer, 2009.
- R. Hielscher, C. B. Silbermann, E. Schmidl, and J. Ihlemann. Denoising of crystal orientation maps. *Journal of Applied Crystallography*, 52:984–996, 2019.
- D. K. Jangid, N. R. Brodnik, M. G. Goebel, A. Khan, S. Majeti, M. P. Echlin, S. H. Daly, T. M. Pollock, and B. Manjunath. Adaptable physics-based super-resolution for electron backscatter diffraction maps. *npj Computational Materials*, 8: 255, 2022.
- M. Kassner. Power-law breakdown and the dislocation microstructure in type 304 stainless steel. *Materials Letters*, 2: 451–454, 1984.
- M. Kassner and R. Ermagan. Power law breakdown in the creep in single-phase metals. *Metals*, 9:1345, 2019.
- M. E. Kassner. *Fundamentals of Creep in Metals and Alloys*. Butterworth-Heinemann, 2015.
- A. A. Mamun, D. Agius, C. A. Simpson, C. Reinhard, C. Truman, M. Mostafavi, and D. Knowles. The effects of internal stresses on the creep deformation investigated using in-situ synchrotron diffraction and crystal plasticity modelling. *International Journal of Solids and Structures*, 229:111127, 2021.
- T. Martinez Ostormujof, R. P. R. Purohit, S. Breumier, N. Gey, M. Salib, and L. Germain. Deep learning for automated phase segmentation in EBSD maps. A case study in dual phase steel microstructures. *Materials Characterization*, 184:111638, 2022.
- T. McAuliffe, A. Foden, C. Bilsland, D. Daskalaki Mountanou, D. Dye, and T. Britton. Advancing characterisation with statistics from correlative electron diffraction and X-ray spectroscopy, in the scanning electron microscope. *Ultramicroscopy*, 211:112944, 2020.
- O. Muránsky, L. Balogh, M. Tran, C. Hamelin, J.-S. Park, and M. Daymond. On the measurement of dislocations and dislocation substructures using EBSD and HRSD techniques. *Acta Materialia*, 175:297–313, 2019.
- N. Otsu. A threshold selection method from gray-level histograms. *IEEE Transactions on Systems, Man, and Cybernetics*, 9:62–66, 1979.
- M. Prager. The omega method—an engineering approach to life assessment. *Journal of Pressure Vessel Technology*, 122: 273–280, 2000.
- V. Randle and O. Engler. *Introduction to Texture Analysis: Macrotecture, Microtexture and Orientation Mapping*. CRC Press, 2000.
- D. Rowenhorst, A. D. Rollett, G. S. Rohrer, M. Groeber, M. Jackson, P. J. Konijnenberg, and M. D. Graef. Consistent representations of and conversions between 3D rotations. *Modelling and Simulation in Materials Science and Engineering*, 23:083501, 2015.
- A. J. Schwartz, M. Kumar, B. L. Adams, and D. P. Field. *Electron Backscatter Diffraction in Materials Science*. Springer, 2009.
- I. Serrano-Munoz, R. Fernández Serrano, R. Saliwan-Neumann, G. González-Doncel, and G. Bruno. Dislocation substructures in pure aluminium after creep deformation as studied by electron backscatter diffraction. *Journal of Applied Crystallography*, 55:860–869, 2022.
- O. D. Sherby and P. M. Burke. Mechanical behavior of crystalline solids at elevated temperature. *Progress in Materials Science*, 13:323–390, 1968.
- B. W. Silverman. *Density Estimation for Statistics and Data Analysis*. Chapman & Hall, 1986.
- S. Subedi, R. Pokharel, and A. D. Rollett. Orientation gradients in relation to grain boundaries at varying strain level and spatial resolution. *Materials Science and Engineering: A*, 638:348–356, 2015.
- S. Takeuchi, K. Fujii, and K. Maeda. Steady state deformation of crystals controlled by motion of screw dislocations. *Journal of the Physical Society of Japan*, 44:1282–1289, 1978.
- S. Van der Walt, J. L. Schönberger, J. Nunez-Iglesias, F. Boulogne, J. D. Warner, N. Yager, E. Gouillart, and T. Yu. scikit-image: Image processing in Python. *PeerJ*, 2:e453, 2014.
- L. Vincent. Morphological grayscale reconstruction in image analysis: applications and efficient algorithms. *IEEE Transactions on Image Processing*, pages 176–201, 1993.
- P. Virtanen, R. Gommers, T. E. Oliphant, M. Haberland, T. Reddy, D. Cournapeau, E. Burovski, P. Peterson, W. Weckesser, J. Bright, S. J. van der Walt, M. Brett, J. Wilson, K. J. Millman, N. Mayorov, A. R. J. Nelson, E. Jones, R. Kern, E. Larson, C. J. Carey, Í. Polat, Y. Feng, E. W. Moore, J. VanderPlas, D. Laxalde, J. Perktold, R. Cimrman, I. Henriksen, E. A. Quintero, C. R. Harris, A. M. Archibald, A. H. Ribeiro, F. Pedregosa, P. van Mulbregt, and SciPy 1.0 Contributors. SciPy 1.0: Fundamental algorithms for scientific computing in python. *Nature Methods*, 17:261–272, 2020.
- B. Wilshire and R. Evans. *Creep Behaviour of Crystalline Solids*. Ashgate Publishing, 1985.
- B. Wilshire and M. Willis. Mechanisms of strain accumulation and damage development during creep of prestrained 316

- stainless steels. *Metallurgical and Materials Transactions A*, 35:563–571, 2004.
- S. I. Wright, M. M. Nowell, and D. P. Field. A review of strain analysis using electron backscatter diffraction. *Microscopy and Microanalysis*, 17:316–329, 2011.
- S. I. Wright, M. M. Nowell, S. P. Lindeman, P. P. Camus, M. De Graef, and M. A. Jackson. Introduction and comparison of new EBSD post-processing methodologies. *Ultramicroscopy*, 159:81–94, 2015.
- P. Yavari, F. A. Mohamed, and T. G. Langdon. Creep and substructure formation in an Al-5% Mg solid solution alloy. *Acta Metallurgica*, 29:1495–1507, 1981.
- J. Zheng and R. D. Hryciw. Segmentation of contacting soil particles in images by modified watershed analysis. *Computers and Geotechnics*, 73:142–152, 2016.

Appendix

The Appendix includes supplementary material that quantifies the data extracted from EBSD images. In particular, it encompasses the assessment of statistical tests to check whether the descriptors, introduced in Section 4, follow different probability distributions for various stress levels and subgrain types. Additionally, the Appendix provides insights into higher moments of the descriptors, specifically standard deviation and skewness.

Statistical tests

To thoroughly validate the visual impression, gained from Fig. 6 to 9 in Section 5, indicating that the descriptors for different subgrain types and stress levels follow distinct distributions, Kolmogorov-Smirnov tests were performed to rigorously assess the statistical differences. These tests aimed to compare different stress levels within a single subgrain type as well as both subgrain types for a specific stress level.

Formally, we check the null hypothesis H_0 if the probability distribution functions F_A and F_B of specific descriptors A and B are equal, e.g. $F_A = F_B$. The statistical tests were conducted with a significance level of $\alpha = 0.05$, i.e., if the p -value of the Kolmogorov-Smirnov test is strictly greater than α , H_0 cannot be rejected. Conversely, if the p -value is less than or equal to 0.05, it suggests that F_A and F_B are (probably) not the same distribution. The p -values of these statistical examinations are presented in Tables A1 to A9, where values are set in bold if the corresponding test failed to reject the null hypothesis. It is noteworthy, that in Tables A1 to A9, red colored cells indicate {001} subgrains, and blue colored cells {111} subgrains. This color code corresponds to Fig. 6 to 9, showcased in Section 5. For instance, in Table A1, a red-colored cell in the column ‘E+A’ and in row ‘29 MPa’ represents the p -value of the Kolmogorov-Smirnov test between {001} subgrains subjected to extrusion+annealing and 29 MPa stress. Similarly, a cell at the intersection of ‘21 MPa’ rows and ‘21 MPa’ columns is colored both blue and red, indicating the test between {111} and {001} grains at a stress level of 21 MPa.

	E+A	21 MPa	29 MPa
E+A	0.0503	0.0	0.0
21 MPa	0.0	0.0	0.0
29 MPa	0.0	0.128	0.0

Table A1: Area $a(S)$

	E+A	21 MPa	29 MPa
E+A	0.5597	0.0	0.0
21 MPa	0.0	0.0	0.005
29 MPa	0.0	0.1628	0.0

Table A5: Length of major axis $\ell_1(S)$

	E+A	21 MPa	29 MPa
E+A	0.0003	0.0	0.0
21 MPa	0.0	0.0	0.0
29 MPa	0.0	0.2166	0.0

Table A2: Length of minor axis $\ell_2(S)$

	E+A	21 MPa	29 MPa
E+A	0.0101	0.0731	0.0004
21 MPa	0.1069	0.3083	0.0024
29 MPa	0.0736	0.5058	0.0124

Table A6: Elongation $e(S)$

	E+A	21 MPa	29 MPa
E+A	0.0037	0.0002	0.5821
21 MPa	0.0	0.0323	0.0231
29 MPa	0.0004	0.0419	0.088

Table A3: Circularity factor $s(S)$

	E+A	21 MPa	29 MPa
E+A	0.002	0.0	0.0
21 MPa	0.0	0.0072	0.0264
29 MPa	0.0	0.0001	0.0889

Table A7: Convexity $c(S)$

	E+A	21 MPa	29 MPa
E+A	0.0043	0.0	0.0
21 MPa	0.0057	0.0027	0.0
29 MPa	0.032	0.6152	0.0017

Table A4: Alignment with Y-axis $\delta(S)$

	E+A	21 MPa	29 MPa
E+A	0.0	0.0	0.0
21 MPa	0.0	0.2952	0.0
29 MPa	0.0	0.0	0.0

Table A8: Intragranular mean misorientation

	E+A	21 MPa	29 MPa
E+A	0.0	0.0	0.0031
21 MPa	0.0	0.0151	0.0
29 MPa	0.0	0.0	0.0

Table A9: Intragranular variance $\sigma^2(S)$

Higher moments

To offer a deeper understanding of the descriptors introduced in Section 4 and elaborated upon in Section 5, additional insights were gained by computing higher moments, namely standard deviation and skewness. The outcomes of these computations are outlined in Tables A10 and A11.

	E+A		21 MPa		29 MPa	
	{001}	{111}	{001}	{111}	{001}	{111}
Area $a(S)$	6.032	4.91	12.338	8.495	11.597	7.518
Length of major axis $\ell_1(S)$	1.709	1.641	2.458	2.153	2.486	2.106
Length of minor axis $\ell_2(S)$	0.889	0.787	1.358	1.052	1.281	0.999
Elongation $e(S)$	0.195	0.197	0.196	0.202	0.201	0.206
Circularity factor $s(S)$	0.079	0.081	0.072	0.078	0.076	0.083
Convexity $c(S)$	0.062	0.064	0.056	0.059	0.057	0.063
Alignment with Y-axis $\delta(S)$	0.289	0.275	0.29	0.294	0.289	0.276
Mean misorientation angle $\mu(S)$	0.268	0.296	0.251	0.229	0.327	0.33
Intragranular variance $\sigma^2(S)$	0.127	0.135	0.126	0.091	0.261	0.208

Table A10: Standard deviations of geometric and crystallographic descriptors.

	E+A		21 MPa		29 MPa	
	{001}	{111}	{001}	{111}	{001}	{111}
Area $a(S)$	2.875	2.28	2.888	3.311	2.951	2.907
Length of major axis $\ell_1(S)$	1.524	1.398	1.637	1.637	1.75	1.53
Length of minor axis $\ell_2(S)$	1.43	1.243	1.666	1.551	1.501	1.503
Elongation $e(S)$	0.423	0.443	0.475	0.373	0.448	0.432
Circularity factor $s(S)$	-0.525	-0.633	-0.721	-0.72	-0.615	-0.74
Convexity $c(S)$	-0.612	-0.732	-1.02	-0.784	-0.76	-0.866
Alignment with Y-axis $\delta(S)$	-0.937	-1.03	-0.879	-0.725	-0.903	-0.911
Mean misorientation angle $\mu(S)$	2.001	1.277	2.063	1.934	2.447	1.377
Intragranular variance $\sigma^2(S)$	11.983	3.835	7.072	6.082	13.865	10.281

Table A11: Skewnesses of geometric and crystallographic descriptors.